

1 **Deep Water Cycling and the Multi-Stage Cooling of** 2 **The Earth**

3 **J. Seales¹, A. Lenardic¹**

4 ¹Department of Earth, Environmental and Planetary Science, William Marsh Rice University, Houston,
5 TX, USA

6 **Key Points:**

- 7 • A change in the deep water cycle can explain Earth's mutli-stage cooling
- 8 • The deep water cycle dominated mantle viscosity during Earth's early evolution
- 9 • A change to thermal effects dominating mantle viscosity occurred around 2.5 Ga.

Corresponding author: Johnny Seales, jds16@rice.edu

Abstract

Paleo-temperature data indicates that the Earth’s mantle did not cool at a constant rate over geologic time. The data suggest slow cooling from 3.8 to 2.5 billion years ago followed by a more rapid cooling until the present. This has been suggested to indicate a change in global tectonics from a single plate to a plate tectonic mode. However, a tectonic change may not be necessary. Multi-stage cooling can result from deep water cycling coupled to thermal mantle convection. Melting and volcanism removes water from the mantle (degassing). Dehydration tends to stiffens the mantle, which slows convective vigor and plate velocities causing mantle heating. An increase in temperature tends to lower mantle viscosity. This increases plate velocities, provided that mantle viscosity offers resistance to plate motion. If these two tendencies are in balance, then mantle cooling can be weak. Breaking this balance, by a switch to net mantle rehydration, can cool the mantle more rapidly. We use coupled water cycling and mantle convection models to test the viability of this hypothesis. Within model and data uncertainty, the hypothesis that deep water cycling can lead to a multi-stage Earth cooling is consistent with present day and paleo data constraints on mantle cooling. It is also consistent with constraints indicating a change from net mantle dehydration to rehydration over the Earth’s geologic evolution. Probability distributions, for successful models, indicate that plate and plate margin strength play a relatively minor role for resisting plate motions relative to the resistance from interior mantle viscosity.

Plain Language Summary

It has been argued that observational constraints on the Earth’s interior cooling indicate that plate tectonics initiated 2.5 billion years ago, with the Earth being a single plate planet, akin to present day Mars and Venus, before that time. The observational constraints are consistent with slow interior cooling from 3.8-2.5 billion years ago followed by an acceleration in cooling rate. That transition does not require a change in the global convective mode of the Earth. It can potentially be explained by changes in the nature of deep water cycling coupled to thermal convection within the Earth’s interior. Under that hypothesis plate tectonics could have operated over the bulk of geologic history, albeit at a variable pace. We use an extensive set of thermal history models to test the viability of the hypothesis that deep water cycling leads to multi-stage Earth cooling. The models indicate that the hypothesis is consistent with present day and paleo constraints on the Earth’s thermal history. The changes in deep water cycling over geologic history, predicted by our successful models, are also consistent with added geochemical constraints on mantle water cycling.

1 Introduction

The rock record helps us unravel the Earth’s geologic history and also its thermal history, i.e., interior cooling over geologic time. Volcanic rocks can be used to estimate mantle temperatures at the time they formed. Figure 1 shows results from several studies that provide constraints on the cooling history of the Earth’s mantle (Ganne & Feng, 2017; Condie et al., 2016; Herzberg et al., 2010). Uncertainty in the paleo data allows for a range of cooling paths. Present day constraints on mantle temperature and the ratio of radiogenic heat generation to mantle heat flow can narrow the range, but multiple model paths remain viable. This being acknowledged, the data trends are suggestive of multi-stage cooling. More specifically, data constraints are consistent with the hypothesis that the mantle experienced a change in cooling slope between 2 and 3 billions of years ago (Condie et al., 2016; Herzberg et al., 2010). That possibility is bolstered by independent studies that indicate changes in the Earth system occurred within the same time window (e.g., Parai & Mukhopadhyay, 2018; Lee et al., 2016; Lyons et al., 2014).

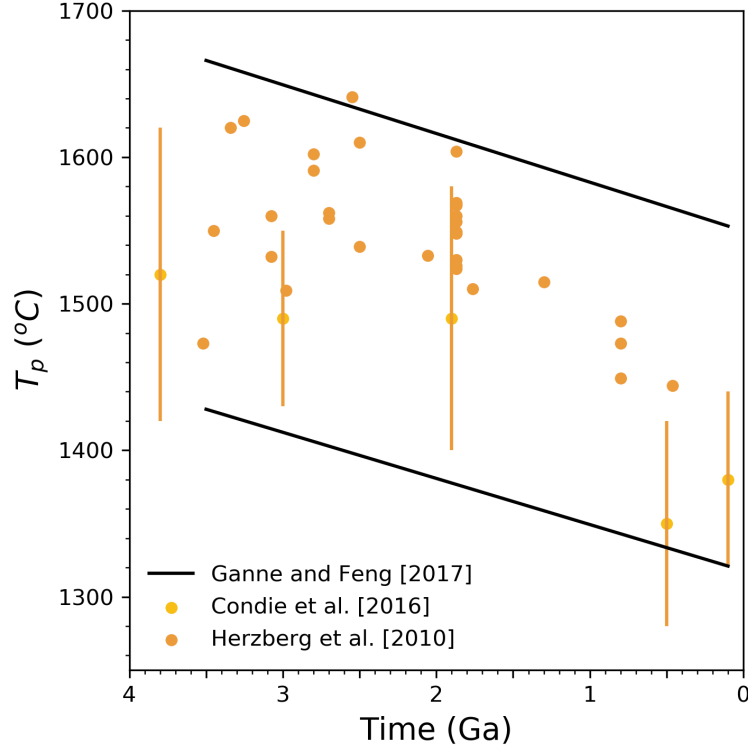


Figure 1. Estimates of Paleo mantle potential temperature.

A conceptual hypothesis for a change in mantle cooling rate at 2.5 billion years ago (Ga) invokes a change from a single plate mode of mantle convection (i.e., stagnant lid convection) to a plate tectonic mode (Condie et al., 2016). To date, thermal history models have not been used to determine the degree to which the hypothesis can match data constraints. Doing so faces challenges from a geodynamical perspective. At present we do not know how long transitions from one convective regime to another would take, over the full range of parameter conditions pertinent to a planets evolution path, and/or the efficiency of mantle cooling through the transition (e.g., Weller & Kiefer, 2020). If transitions are as long as Weller and Kiefer (2020) argued for (potentially a billion year time scale), then globally averaged heat balance models would be inapplicable and 3-D numerical simulations would be needed to map thermal histories. Running such models over geologic time scales is computationally intensive and requires large amounts of wall time, particularly if we also require model uncertainty quantification. This is not insurmountable, but it is not the only option.

Invoking tectonic transitions may be an intuitive way to account for changes in the Earth's cooling rate. It is not, however, the only one. There are alternative hypotheses that do not invoke tectonic transitions. That class of hypotheses does not violate critical assumptions of globally averaged thermal history models; i.e., parameterized thermal history models (Schubert et al., 1980; Davies, 1980). Such models allow for efficient hypothesis testing as mapping of parameter space, and associated uncertainty quantification, is not subject to computational and wall time restrictions that come with 3-D numerical simulations. One specific alternative invokes increasing plate strength in the Earth's past (Korenaga, 2003). That hypothesis assumes that the resistance to plate motion comes from plate strength. This is a break from classic thermal history models which are based on the idea that mantle viscosity dominates resistance to plate motion (Tozer,

1972). Thermal history models based on increasing plate strength in the past have been used to show that the hypothesis can lead to a multi-stage thermal history. The change in mantle temperature slope over time they predict is more extreme than a change in cooling slope at ~ 2.5 Ga. The models predict a change in the sign of the slope with the mantle heating before the transition and cooling after it. Less extreme versions of this hypothesis, that still assume plate strength dominates resistance to plate motion but not that it increases in the past, can also lead to changes in cooling rate over time (Christensen, 1984; Conrad & Hager, 1999b).

A systematic study that ran over one million thermal history models, with variable assumptions as to plate resisting forces, showed that models invoking plate strength as dominating resistance to plate motion showed peaks in the probability distribution of model cases that could account for observational constraints (Seales & Lenardic, 2020). That is, such models are successful (the principal objective measure of model success being its ability to account for the observations it sets out to model). However, the physical validity of the plate resistance parameterizations used within such models has not been confirmed (Gerardi et al., 2019). The physical validity of a parameterization that assumes internal viscosity offers the dominant resistance to convective and associated plate motion has, on the other hand, been confirmed via experiments (e.g., Giannandrea & Christensen, 1993) and numerical simulations (e.g., Schubert & Anderson, 1985; Lenardic & Moresi, 2003; Gurnis, 1989). This does not over-ride the ability of plate strength models to account for observations. It does, however, suggest the question of whether a class of hypotheses that does not hinge on plate strength resisting plate motion can also lead to multi-stage cooling.

Classic thermal history models assume that mantle viscosity resists plate motion and that mantle viscosity is a function of temperature. This leads to a strong negative feedback (Tozer, 1972). As a result, the thermal paths for such models rapidly settle on a near constant cooling path over geologic time (Schubert et al., 1979). However, mantle viscosity also depends on hydration (e.g., Karato & Wu, 1993). Mantle hydration effects allow for water cycling feedbacks to interact with thermal feedbacks and variations in the strength of the feedbacks allows for different mantle cooling rates (Crowley et al., 2011; Sandu et al., 2011). Resistance to plate motion still comes from mantle viscosity, but the viscosity is no longer determined solely by a thermal feedback.

In this paper we will test the ability of a deep water cycling hypothesis to account for thermal history data constraints with a focus on how changes in coupled water cycling and thermal feedbacks can lead to multi-stage cooling. More specifically, we will explore the hypothesis that a change from net mantle dehydration to net mantle rehydration can cause an increase in mantle cooling rates consistent with paleo data constraints. This specific add on is based on the feedback analysis of Crowley et al. (2011). Those authors argued that a net dehydrating mantle could drive a component of mantle heating, which could compete with thermally driven cooling. They showed the opposite for a net rehydrating mantle. The hypothesis is also based on a geochemical argument that showed the Earth has transitioned from net dehydrating mantle to net rehydrating mantle over geologic time (e.g., Parai & Mukhopadhyay, 2018). In the next section we define our model and discuss the model's feedback structure. We then present model results and discuss implications for the Earth's coupled thermal and deep water cycling history.

2 Methods

In this section we define the coupled model we use, discuss the observational data constraints applied to model outputs, and provide an overview of the feedback structure associated with this model.

2.1 Coupled Deep Water Cycling and Thermal History Model

Figure 2 shows a cartoon of how our model works conceptually. Plate generation and subduction cools the interior mantle and also cycles water between mantle and surface reservoirs. Mantle viscosity, which effects the vigor of mantle convection and associated mantle cooling, depends on both temperature and mantle hydration. This leads to coupled thermal and water cycling feedbacks on mantle viscosity and, by association, mantle cooling. Variations in the strength of each feedback over geologic time allows for the potential of differing cooling efficiencies. We lay out the coupled model starting with the thermal component, then moving to the water cycling component, and then defining the mantle viscosity function that provides a coupling between the two.

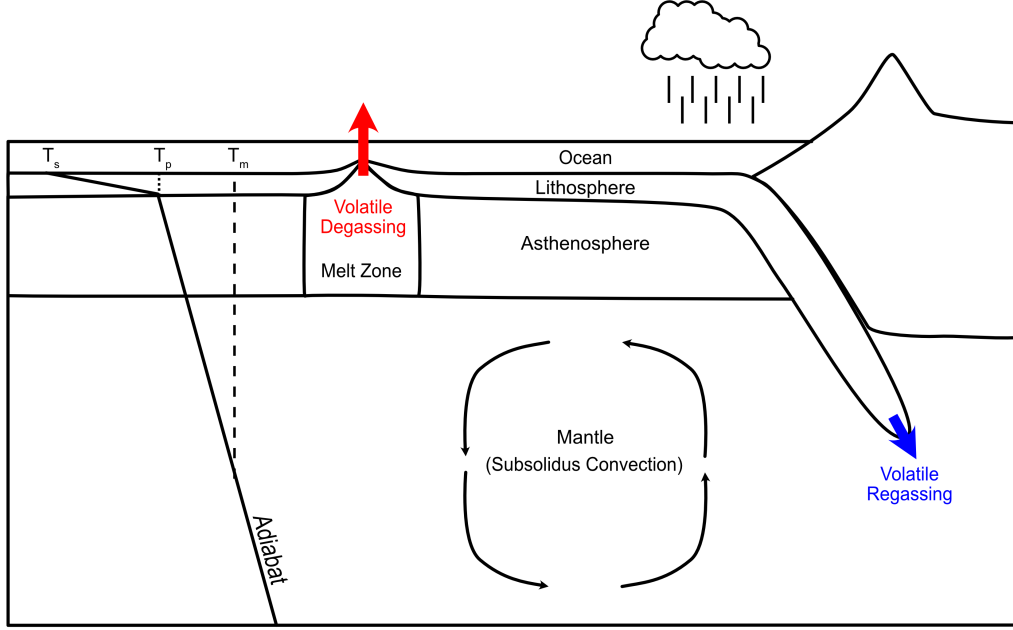


Figure 2. Cartoon schematic of the coupled thermal and deep water cycle model.

2.1.1 Thermal Component

We used a parameterized thermal history model (Schubert et al., 1979, 1980) to track how Earth’s mantle temperature (T_m) changed with time. This model is a global energy balance expressed as

$$\rho C(R_m^3 - R_c^3)\dot{T}_m = -3(R_m^2 - R_c^2)q_m + (R_m^3 - R_c^3)Q(t) \quad (1)$$

where ρ is mantle density, C is mantle heat capacity, and q_m is the mantle surface heat flux. R_m is the radial distance from Earth’s center to the surface, and R_c is the radial distance to the Core-Mantle-Boundary (CMB). We define the Urey ratio (Ur) here

$$Ur = \frac{(R_m^3 - R_c^3)Q}{3(R_m^2 - R_c^2)q_m}, \quad (2)$$

since we use it later as a model constraint.

The decay of radiogenic elements produces heat within the the mantle ($Q(t)$) according to

$$Q(t) = Q_0 e^{-\lambda t}, \quad (3)$$

where Q_0 and λ are constants, and t is time in millions of years.

The Rayleigh number (Ra) is the ratio of forces driving convection to those resisting it. It is defined as

$$Ra = \frac{\rho g \alpha \Delta T Z^3}{\eta \kappa} \quad (4)$$

where g , α , Z , η and κ are gravity, thermal expansivity, depth of the convecting layer, viscosity and thermal diffusivity, respectively. The value ΔT is the temperature difference driving convection defined as $T_m - T_s$, where T_s is surface temperatures. In parameterized thermal history modeling heat flux from the mantle is typically solved for using the Nusselt-Rayleigh scaling (Schubert et al., 2001), where the Nusselt number (Nu) is a nondimensional heat flux. The scaling takes the form

$$Nu = \frac{q_m Z}{k \Delta T} = \left(\frac{Ra}{Ra_{cr}} \right)^\beta \quad (5)$$

Equation 5 is used to solve for q_m . In Equation 5, k is thermal diffusivity, Ra_{cr} is the critical Rayleigh number, which determines the onset of convection, and β is a scaling exponent.

The choice of β in Equation 5 has a rich history. The earliest thermal history models used a value of 0.33 (Schubert et al., 1980; Spohn & Schubert, 1982; Jackson & Pollack, 1984). This assumes that mantle viscosity provides the dominant resistance to plate motion (Tozer, 1972). It also assumes very vigorous convection. For levels of convection pertinent to the Earth the scaling exponent is slightly lower, $0.30 \leq \beta \leq 0.32$ (Schubert & Anderson, 1985; Lenardic & Moresi, 2003; Moore & Lenardic, 2015). Models that more directly incorporated analogues to tectonic plates, showed that values nearly matching this scaling would be recovered provided that weak plate boundaries were also incorporated (Gurnis, 1989). Later models that allowed weak plate boundaries to develop dynamically lead to a scaling exponent of 0.29 (Moresi & Solomatov, 1998). If plate boundaries are not so weak that energy dissipation along them can be neglected and/or if plate strength offers significant resistance, then the scaling exponent has been argued to be lower with a range between $0 \leq \beta \leq 0.15$ having been proposed (Christensen, 1985; Giannandrea & Christensen, 1993; Conrad & Hager, 1999a, 1999b). A low viscosity channel below plates - the Earth's asthenosphere - allows different size plates to have different balances between driving and resisting forces (Crowley et al., 2011; Höink et al., 2011). This leads to a mixed mode scaling. For the current distribution of plate sizes, the mixed mode leads to a global heat flow scaling exponent of 0.20 (Höink et al., 2013). Korenaga (2003) made an argument for $\beta < 0$. The physical basis for $\beta < 0$ is that at hotter mantle temperatures enhanced melting would generate a thicker dehydrated layer below oceanic crust. This layer would be responsible for the bulk of plate strength. By this reasoning, hotter mantle temperatures in Earth's past would allow for thicker, stronger plates, which would slow plate velocities and decrease the rate at which the mantle cooled.

As noted in the introduction, our goal is to explore models that do not rely on plate strength and/or plate margin strength providing the dominant resistance to plate motions. As such, we will not consider models with $\beta < 0.20$. We will not, however, assume an *a priori* preferred β value. Rather, we will test a range of models with $0.2 \leq \beta \leq 0.33$ at intervals of 0.01.

In defining a velocity scale (u_c), we first rearranged Fourier's law to determine lithospheric thickness (D_b)

$$D_b = k \frac{(T_b - T_s)}{q_m} \quad (6)$$

In Equation 6 k is thermal conductivity. The temperature T_b is the temperature at the base of the lithosphere. Using boundary layer theory (Schubert et al., 2001) we calculated the boundary layer breakaway time associated with subducting lithosphere accord-

ing to

$$t_s = \frac{1}{5.38\kappa_m} D_b^2. \quad (7)$$

Finally, we defined u_c as

$$u_c = \frac{(R_m - R_c)}{t_s}, \quad (8)$$

This is of the form $u_c \sim Ra^{2\beta}$. More precisely:

$$u_c = \frac{a_1\kappa}{2(R_m - R_c)} \left(\frac{Ra}{Ra_{crit}} \right)^{2\beta}. \quad (9)$$

Here a_1 is a scaling parameter. It takes the value of 5.38 for the case where $\beta = 1/3$ (Schubert et al., 1979, 1980). For simplicity, we assumed this holds for all tested β values. To achieve consistent velocities at present day mantle temperatures, we accounted for the effect of β on u_c . We used the present day values for convective vigor (Ra_{now}) and velocity (u_{now}) along with the $\beta = 1/3$ scaling used as a reference. This gave us

$$u_{now} = a_1 \frac{\kappa}{2(R_m - R_c)} \left(\frac{Ra_{now}}{Ra_{crit}} \right)^{\frac{2}{3}} \quad (10)$$

$$u_{now} = a_2 \frac{\kappa}{2(R_m - R_c)} \left(\frac{Ra_{now}}{Ra_{crit}} \right)^{2\beta} \quad (11)$$

$$a_2 = a_1 Ra_{crit}^{2\beta - \frac{2}{3}} Ra_{now}^{\frac{2}{3} - 2\beta}, \quad (12)$$

where we calculated the value of a_2 for each β . Equation 10 holds for $\beta = 1/3$ and equation 11 holds for all other tested values of β .

2.1.2 Deep Water Cycle Component

The deep water cycling component tracked the flow of water between the surface and interior reservoirs. We used the model of Sandu et al. (2011). Water leaves the mantle as an incompatible element via batch melting. We assumed that melting at mid-ocean ridges dominated water loss from the mantle. Subducting slabs deliver water back into the mantle. In the following we detail how we tracked these flows.

Melting We tracked mantle melting by defining a geotherm, a solidus and a liquidus. We assumed the geotherm was in conductive equilibrium in the lithosphere and followed the adiabat below this

$$T(z)|_{z \leq D_b} = T_s + \frac{q_m}{k} z. \quad (13)$$

$$T(z)|_{z > D_b} = T_p + \frac{g\alpha T_m}{C_p} z. \quad (14)$$

In equations 13 and 14, the potential temperature (T_p) is mantle temperature minus the adiabatic component and is calculated at the base of the lithosphere. We would like to emphasize that a depth dependent thermal profile in the interior mantle is used to calculate melt volumes only; in our models, adiabatic heating does not drive convection.

The solidus defines the temperature vs. depth profile below which all mantle material will remain in its solid phase. If the mantle is warmer than the solidus, it will start to melt. Increasing mantle temperature further increases the volume of melt produced. If temperature increases enough, the entire parcel of mantle melts. This temperature defines the liquidus. We used two second-order polynomial curves to define the solidus and liquidus (Hirschmann, 2000). For hydrous melting these functions are

$$T_{sol-hydr} = T_{sol-dry} - \Delta T_{H_2O} \quad (15)$$

$$T_{liq-hydr} = T_{liq-dry} - \Delta T_{H_2O} \quad (16)$$

where $T_{sol-dry}$ and $T_{liq-dry}$ are the dry solidus and liquidus, respectively. $T_{sol-hydr}$ is the hydrated solidus and $T_{liq-hydr}$ is the hydrated liquidus. In equations 15 and 16, the second term represents the temperature shift of each curve caused by hydrous melting. This adjustment temperature scales with water concentration in the melt according to

$$\Delta T_{H_2O} = K X_{melt}^\gamma \quad (17)$$

where K and γ are constants, which were calibrated by (Katz et al., 2003). The parameter X_{melt} is the ratio of water in the melt fraction expressed in kg of water per kg of melt. It is calculated as

$$X_{melt} = \frac{C_{mv}}{D_{H_2O} + F_{melt}(1 - D_{H_2O})}. \quad (18)$$

In Equation 18, C_{mv} is the bulk water composition in the solid mantle (expressed as a weight fraction), and D_{H_2O} is the bulk distribution coefficient which takes the value of 0.01 – highlighting it behaves as an incompatible trace element. The term F_{melt} is the degree of melting expressed as melt fraction. It is parameterized by a power-law as

$$F_{melt} = \frac{T - (T_{sol-dry} - \Delta T_{H_2O}(X_{melt}))^\beta}{T_{liq-dry} - T_{sol-dry}}. \quad (19)$$

This definition of F_{melt} is valid from the surface to a depth of 300 km as constrained by observation and melting experiments. Therefore, we prohibited any melt production below this depth.

The melt zone thickness D_{melt} is dependent upon the relative positioning of the geotherm and the solidus. The base of the melt zone is the deepest temperature at which these curves intersected. At this depth, a parcel of upwelling mantle starts melting. The top of the melt zone is where geotherm and solidus intersect closer to the surface. At this depth, the parcel of mantle has cooled to the point where melt is no longer produced. The vertical distance between these two depths defines D_{melt} . We integrated F_{melt} and C_{mv} over D_{melt} to provide average values for our water budget calculations.

Degassing Melting at mid-ocean ridges (MOR) transfers water from the mantle reservoir to the surface reservoir. The degassing rate (r_{MOR}) depended on the volume of mantle moving through the melt zone, the amount of melt produced within the melt zone, and how much of the water within the melt makes it to the surface. We modeled this process as

$$r_{MOR} = \rho_m F_{melt} X_{melt} D_{melt} S \chi_d \quad (20)$$

where F_{melt} is the integrated melt fraction in the melt zone and χ_d is the degassing efficiency factor. Both D_{melt} and X_{melt} are calculated as specified above. The areal spreading rate (S), which is derived from a boundary layer model (Schubert et al., 2001), is defined as

$$S = 2L_{ridge}u_c. \quad (21)$$

We have assumed symmetrical spreading along a constant ridge length (L_{ridge}) and use the definition of u_c given in equation (8).

Regassing Subducting slabs deliver water bound in the serpentinized and thin sedimentary layers back into the mantle (Rüpke et al., 2004). We assumed that most water held in the sedimentary layer degassed from the slab and found its way back to the surface. Therefore, we only accounted for water delivered by the serpentinized layer. Water was delivered back into the mantle at a rate of

$$r_{SUB} = f_h \rho D_{hydr} S \chi_r, \quad (22)$$

where f_h , D_{hydr} , and χ_r are the mass fraction of water in the serpentinized layer, the thickness of the serpentinized layer and the regassing efficiency factor, respectively. The hydrous phase of serpentinite decomposes at a temperature around 700 °C (Ulmer & Trommsdorff, 1995). We calculated the depth of this isotherm in the subducting slab (D_{hydr}). We assumed the maximum value D_{hydr} could take was 20 km. This is a rough approximation of the depth to which fractures may penetrate and deliver water into the lithosphere during slab bending at convergent margins.

We calculated the flow rate of mantle water (r_{Mmv}) according to

$$r_{Mmv} = r_{SUB} - r_{MOR}. \quad (23)$$

Positive values of r_{Mmv} indicate a net influx of water into the mantle.

2.1.3 Temperature- and Water-Dependent Mantle Viscosity

The temperature dependence of mantle viscosity is defined as:

$$\eta = \eta_0 \exp\left(\frac{A}{RT_m}\right) \quad (24)$$

where η_0 , A , R are a reference viscosity, activation energy for dislocation creep (Weertman & Weertman, 1975) and the universal gas constant, respectively. The amount of water in the mantle also played a role in determining mantle viscosity. Experiments have shown that mantle viscosity and mantle water volumes are related by a power-law (Carter & Ave'lallemant, 1970; Chopra & Paterson, 1984; Mackwell et al., 1985; Karato & Wu, 1993). The power law was further refined to include dependence on water fugacity in olivine (Hirth & Kohlstedt, 1996; Mei & Kohlstedt, 2000). Assuming an empirical relation for water fugacity based on mantle water concentrations (Li et al., 2008), we calculate the effective viscosity as

$$\eta_{eff} = \frac{\tau}{\dot{\epsilon}} = \eta_0 A_{cre}^{-1} \left(\exp(c_0 + c_1 \ln C_{OH} + c_2 \ln^2 C_{OH} + c_3 \ln^3 C_{OH}) \right)^{-r} \exp\left(\frac{A}{RT}\right) \quad (25)$$

where τ is stress and $\dot{\epsilon}$ is strain rate. Li et al. (2008) determined the constants c_0 , c_1 , c_2 and c_3 . The water concentration (C_{OH}) is expressed in $H/10^6$ Si. The values η_0 and A_{cre} are a calibration and material constant, respectively. Table 1 lists the values of the fixed parameters we used in our study. Table 2 lists the parameter space we tested.

2.2 Analyzing Structural Stability

A model is structurally stable if its outputs do not qualitatively change in the presence of low amplitude unmodeled effects (Guckenheimer & Holmes, 1983; George & Oxley, 1985). Applying structurally unstable models to account for observational data sets is problematic as the robustness of conclusions will be compromised. For this reason, the first step we took in testing our model was to determine whether it was structurally stable. We assessed structural stability using a “perturbed physics” approach (Astrom & Murray, 2008). Our approach followed the specifics detailed in Seales et al. (2019). In short, we randomly perturbed the model over time. Perturbations were randomly drawn from a normally distributed set that had a fixed mean and variance. We repeated this process 100 times to form an ensemble of perturbed paths. Each perturbed path started with an identical initial condition and had the same parameter values. However, as the perturbations were random, the perturbed paths differed from each other. To determine whether the model was structurally stable, we compared the mean of the ensemble to the unperturbed path. If the two are within some tolerance, the model is structurally stable.

For a structurally stable model, we can relate the ensemble spread to the model’s structural uncertainty (Strong & Oakley, 2014; Wieder et al., 2015). The structural un-

Table 1. Deep Water Cycle Model Parameters

Model	Parameter	Description	Value	Units
Convective Model	T_s	Surface temperature	300	K
	$H(0)$	Initial radiogenic heat	4.51	$J/(m^3 yr)$
	R_m	Mantle radius	6371	km
	R_c	Core radius	3471	km
	ρ_m	Mantle density	3000	kg/m^3
	k_m	Thermal conductivity	4.2	$W/(mK)$
	cp	Specific heat	1400	$J/(kgK)$
	α	Thermal expansivity	3.00×10^{-5}	K^{-1}
	β	Convective exponent	0.33	-
	λ	Decay constant	3.4×10^{-10}	yr^{-1}
	Ra_{cr}	Critical Rayleigh number	1100	-
Water Cycling	η_0	Viscosity constant	1.7×10^{17}	Pa.s
	A_{cre}	Material constant	90	$MPa^{-r/s}$
	r	Fugacity exponent	1.2	-
	Q_a	Creep activation energy	4.8×10^5	J/mol
	χ_d	Degassing efficiency factor	0.03	-
	χ_r	Regassing efficiency factor	0.015	-
	OM	Mass of 1 Earth ocean	1.39×10^{21}	kg
	OM(0)	Ocean masses initially in mantle	2	-

Table 2. Tested Parameter Space

Parameter	Description	Values
β	Convective exponent	0.2-0.33
H_i	Initial radiogenic heat	4.51, 3.157
T_{m_i}	Initial mantle temperature	3300, 2300, 1300
χ_d	Degassing efficiency factor	0.002, 0.02, 0.04, 0.4
χ_r	Regassing efficiency factor	0.001, 0.003, 0.01, 0.1
OM_i	Ocean masses initially in mantle	0.01, 0.25, 0.5, 0.75, 1, 2, 4, 6

certainty of the model is the time dependent form of the ensemble. It provides a probability distribution of how far the perturbed paths stray from the mean (in effect, it is a model confidence interval that accounts for structural uncertainty). For the purposes of our study, we define the structural uncertainty bounds as the two-sigma window from the full ensemble about the mean path (further details can be found in Seales et al. (2019) and Seales and Lenardic (2020)).

2.3 Observational Data Constraints

Successful models are defined as those that can satisfy observational constraints. We use both present day and paleo proxy data to constrain successful model paths. For present day constraints, we use mantle temperature and Ur (Equation 2). The present day mantle temperature falls between 1300 and 1400 C (Herzberg et al., 2010). Jaupart et al. (2007) estimated the present day Ur is between 0.2 and 0.5. Accounting for the

thermal effect of continents allows for an upward Ur correction of 0.2 (Lenardic et al., 2011; Grigné & Labrosse, 2001).

Figure 1 shows paleo temperature proxy data constraints. The upper and lower bounds of Ganne and Feng (2017) encompass the data sets of Condie et al. (2016) and Herzberg et al. (2010). Ganne and Feng (2017) suggested that their maximum and minimum bounds may represent the temperature of plumes and ambient mantle, respectively. This is not consistent with Condie et al. (2016) Herzberg et al. (2010), who both considered their data to represent ambient mantle (which would correlate to T_p for thermal history models). We will do the same herein. Under this view the combined data spread, from different groups, represents observational uncertainty in paleo temperature constraints.

The full range of observational uncertainty allows multiple models to be viable (Seales & Lenardic, 2020). As noted in the introduction, our aim is to test the idea that the Earth experienced a multi-stage cooling. As such, we will follow the conceptual interpretation of the data offered by Condie et al. (2016), who argued that the data was indicative of a change in cooling slope at 2.5-2.0 Ga. Our specific hypothesis for this change in slope is a change from net mantle dehydration to rehydration. For this reason our successful models will not only need to match thermal data, within uncertainty, but will also need to allow for a change in net hydration between 3.0 to 1.75 Ga and an associated change in cooling slope (or potentially a change from heating to cooling) within that time window.

2.4 First Order Model Feedbacks

Before moving to model results, it is worth conceptually overviewing critical model feedbacks. In our models, we assumed that mantle viscosity was the dominant resistor to plate motions. As shown in Equation 25, both mantle temperature (T) and mantle water concentration (χ_m) influence mantle viscosity (η). Figure 3 shows a feedback loop diagram for coupled hydration and thermal feedbacks (Crowley et al., 2011). The left hand side of Figure 3 shows the thermal feedback structure. If mantle temperature were to increase, mantle viscosity would decrease. This would increase plate velocities. Faster velocities increases heat flow and cool the mantle. An increase in mantle temperature results in mantle cooling, a negative feedback. Therefore, the thermal part of our model wants to buffer itself from changes as has been known for some time (Tozer, 1972).

The right hand side of Figure 3 shows the water cycling feedback loop. Mantle viscosity effects both the thermal and the water cycling loop which leads to a coupling between the two. If there is a net flow of water out of the mantle, χ_m decreases. Removing water from the mantle increases mantle viscosity. This causes plates to move more slowly, decreasing mantle heat flow. This results in a hotter mantle, which has two effects on water transport. First, a hotter mantle is associated with a thinner lithosphere. Thinning the lithosphere also thins the hydrated layer held within it. A thinner hydrated layer can deliver less water back into the mantle. A second effect of a hotter mantle is that it decreases the solidus, which generates more melt. Both decreased return of water to the mantle and increased melting by a depressed solidus cause a net decrease in mantle water concentration. The water cycle feedback, then, introduces the potential of a positive feedback. If water is lost, feedbacks can lead to a tendency to lose more. This positive feedback can dominate the overall system feedback if it is not offset or balanced by the thermal feedback. Which type of behavior will prevail depends on the strength balance between the feedbacks which can change over time. For this reason we will need to be able to quantify the strength of different feedbacks over model evolution times.

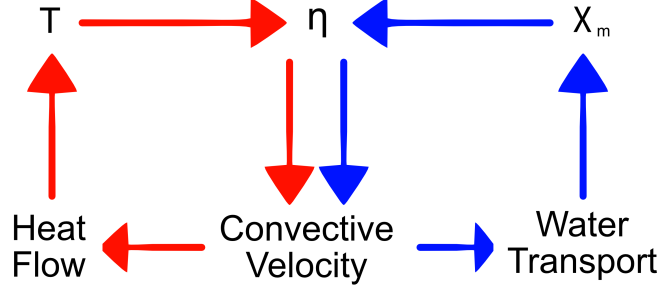


Figure 3. Simplified feedback loops associated with the thermal (negative feedback) and deep water cycle (positive feedback) modules of the coupled model.

2.5 Assessing Feedback Strengths

Testing the hypothesis that a change in the deep water cycle can account for a multi-stage thermal history requires that the strength of feedbacks over model evolution time can be quantified. We will do so using the method developed by Crowley et al. (2011). The method determines which feedback, thermal or water cycling (Figure 2), dominated mantle viscosity at a particular time. The method defines the change of mantle viscosity ($\dot{\eta}$) as a function of these feedback as

$$\dot{\eta} = \frac{\partial \eta}{\partial T} \frac{\partial T}{\partial t} + \frac{\partial \eta}{\partial \chi_m} \frac{\partial \chi_m}{\partial t} = \eta_T \dot{T} + \eta_\chi \dot{\chi}_m. \quad (26)$$

The first term on the right hand side ($\eta_T \dot{T}$) represents the thermal feedback and the second term ($\eta_\chi \dot{\chi}_m$) the water cycling feedback. In our forward model, we solve for \dot{T} from equation 1 and $\dot{\chi}_m$ using equation 23. We can calculate η_T and η_χ by taking partial derivatives of equation 25, which are

$$\eta_T = -\frac{A\eta}{RT_m^2}. \quad (27)$$

$$\eta_\chi = -\frac{r\eta}{\chi_m} (c_1 + 2 * c_2 \ln(C_{OH}) + 3 * c_3 \ln^2 C_{OH}). \quad (28)$$

Crowley et al. (2011) defined a nondimensional ratio of these two values

$$S_{WT} = \left| \frac{\eta_\chi \dot{\chi}_m}{\eta_T \dot{T}} \right|. \quad (29)$$

When $S_{WT} > 1$ the water cycling feedback starts to dominate. For lower values, the thermal feedback becomes progressively more dominant in the overall feedback structure. Using the outputs of our model, we determined time intervals with different feedback structures. Doing so allowed us to more fully quantify our principal hypothesis.

3 Results

In this section we assess model structural stability, isolate model paths that satisfy geologic proxy data (from more than 10^5 model paths with variable initial conditions, model inputs, and β values, see Table 2), and analyze the degree to which coupling deep water cycling to the Earth's thermal evolution can account for a multi-stage cooling history.

3.1 Structural Stability and Structural Uncertainty

Figure 4a shows the structural uncertainty of a coupled model compared to that of a thermal history model with no water cycling (Seales et al., 2019). Each model is for $\beta = \frac{1}{3}$. Coupling the deep water cycle to the thermal history model caused a four fold increase in the structural uncertainty. The uncertainty maxed out at a two-sigma value of $\sim 100^\circ\text{C}$ at present day.

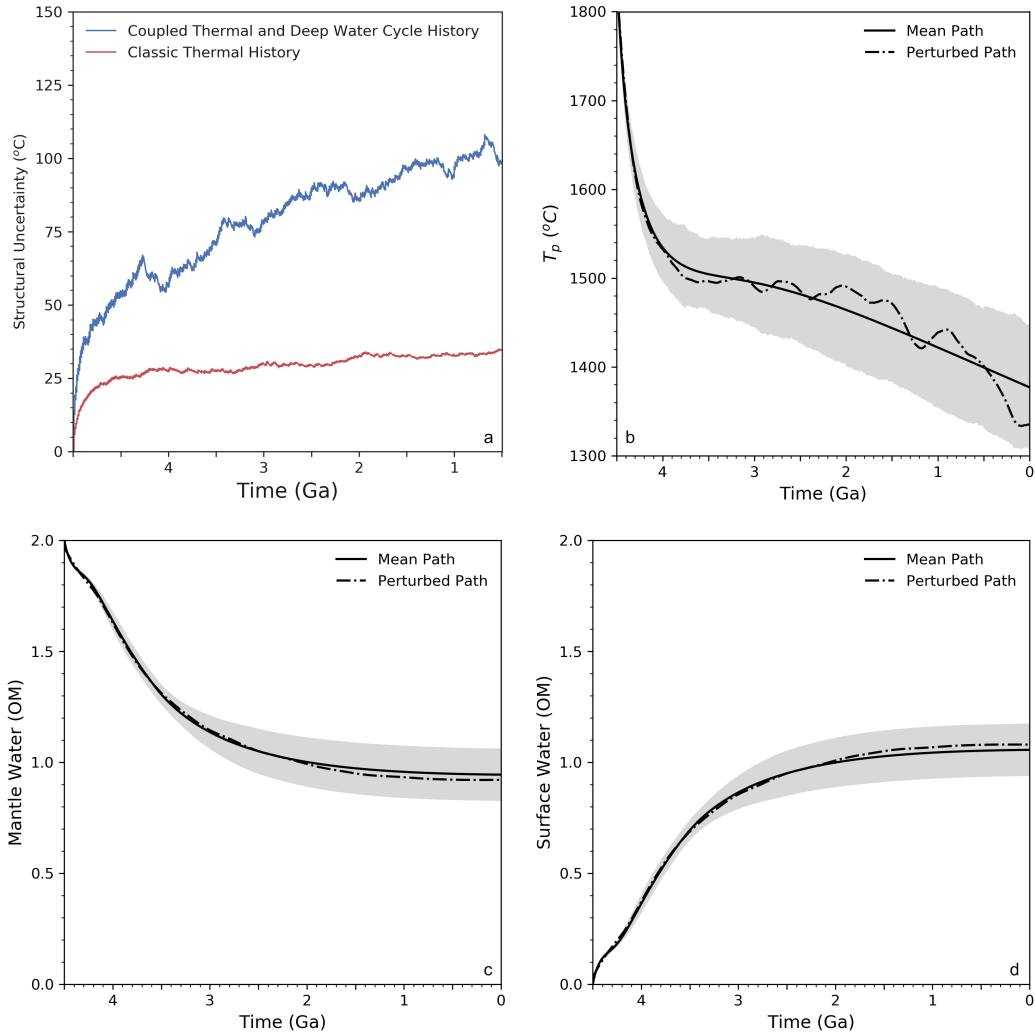


Figure 4. Structural uncertainty analysis. a) Comparison of simple and coupled thermal history model structural uncertainties. b) Sample thermal history ensemble and one ensemble path. c) Mantle water volume ensemble with structural uncertainty. d) Surface water volume ensemble with structural uncertainty.

Figure 4b plots a structural uncertainty window for a model path (shaded gray). The window is determined from 100 different perturbed cases of the coupled model used for Figure 4b. This provides, in effect, a structural confidence interval for a model path. The solid line shows the ensemble mean from all the perturbed cases. The ensemble mean matched the evolution path of the unperturbed model which indicated that the model maintains structural stability. We also show one perturbed path from the ensemble (dashed line). It retained the same first order trend of the mean path. The structural uncertainty for present day temperature was very near the uncertainty in present day data constraints. For paleo temperatures, structural uncertainty was less than the uncertainty associated with paleo proxy data constraints.

In Figure 4c and 4d we show the ensemble window for both mantle and surface water volumes, respectively. Each water volume ensemble is for the thermal path shown in Figure 4c. The structural stability of the model lead to the mean of ensemble paths tracking the unperturbed model path. For water volumes, individual perturbed paths more closely tracked means values than was the case for mantle temperature. The structural uncertainty for water volumes maxed at $\sim 11\%$.

What is critical, in terms of model application, is that our uncertainty analysis shows that the structural uncertainty of our model is comparable to uncertainty in present day data and is smaller than the uncertainty of proxy paleo data. If this was not the case, and the structural uncertainty of a model was considerably greater than that of observational constraints, then the ability of constraints to knock out model (i.e., rule out hypotheses) would be weakened. In effect, models with high levels of structural uncertainty relative to data become harder to rule out using the data itself. This is not the case for our models over the β range we will test. For lower β value models, particularly negative β models, this is no longer the case as structural uncertainty can be larger than data uncertainty (Seales et al., 2019). This is another reason why we focused on higher β models.

The perturbed paths that make up the ensemble provide a proxy means for modeling shorter time-scale fluctuations about a mean thermal history trend (Lenardic et al., 2016). Our interest herein is on whether distinct cooling stages are possible over geologic time. If so, these stages would show different means. Our structural uncertainty analysis shows that, for a structurally stable model, that will hold in light of low amplitude, unmodelled effects. As such, we will focus the results section on mean trends. In terms of assessing the ability of models to match data constraints, using mean trends will rule out a larger class of models as accounting for structural uncertainty would increase the probability that any particular case could match data. That increase would scale as the structural uncertainty of the model. We will take the more restrictive approach in testing our main hypothesis noting that structural uncertainty allows for an extended range of successful model paths.

3.2 Models That Match Observational Data Constraints

Observational constraints were used to eliminate unsuccessful model paths. By model path we mean the thermal path we computed using a unique set of initial condition and parameter values for models with different values of β . We applied different constraints individually to all model paths. This provided a distribution of model paths that satisfied each constraint (Figure 5 and 6). Figure 5 shows the distribution of model paths that satisfied the present day T_p constraints (Figure 5a) and present day Ur constraints (Figure 5b). Figure 6 shows the distribution of model paths that satisfied the paleo proxy data constraints. Figure 6a is the most conservative paleo constraint applied as models only needed to fall within the full range of observational uncertainty (Figure 1). The constraint of Figure 6b provides a less conservative paleo constraint as it also rules out

models that do not allow for a changes in mantle hydration from net degassing to regassing
between 3.0 and 1.75 Ga.

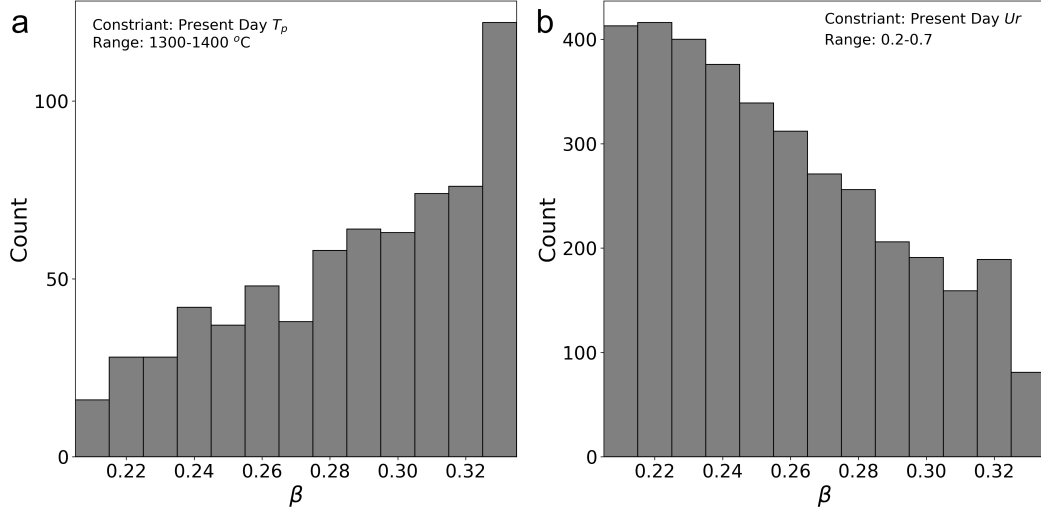


Figure 5. Distributions of model paths that matched paleo constraints: a) thermal and b) change to a net rehydrating mantle.

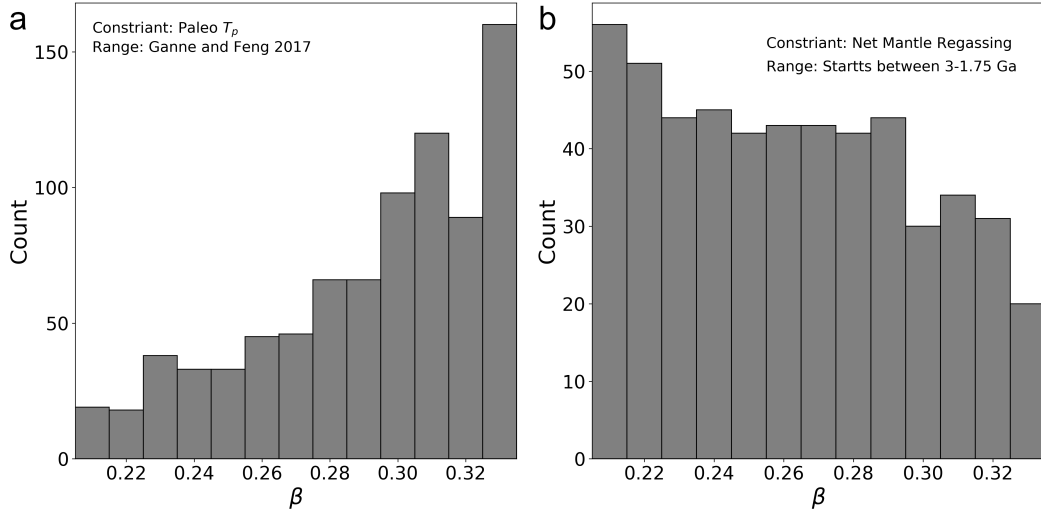


Figure 6. Distributions of model paths that matched present day constraints: a) thermal and b) Ur

Each constraint eliminated different paths, which progressively decreased the number of successful paths. Figure 7 shows the distribution of model paths that satisfied all constraints (Figure 7). The paths are distributed between a minimum β value of 0.25 and a maximum of 0.3, peaking around $\beta = 0.29$. Figures 5 and 6 hinted at this outcome. In both the paleo and present day proxy data, one constraint favored paths with a higher β value whereas the other favored paths with a lower β value. This indicated

the likelihood of a sweet spot. When we inspected the parameters of the successful paths, we found a commonality between 19 of 21: the value of $\chi_d = 0.04$ and $\chi_r = 0.1$.

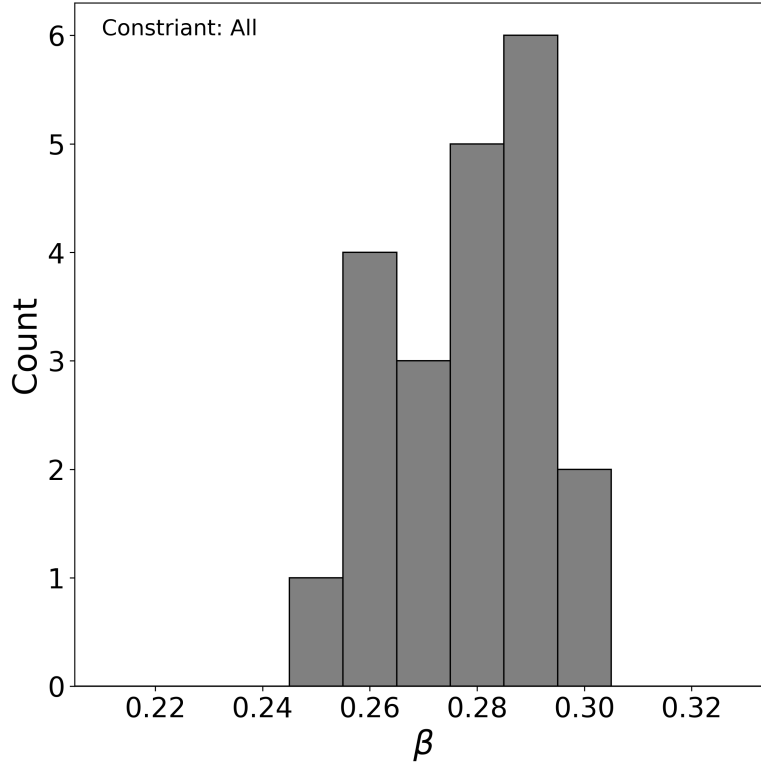


Figure 7. Distribution of model paths that matched all constraints.

Figure 8 shows the present day mantle and surface water volumes associated with the thermal paths that matched all thermal constraints. Paths that assumed initial mantle water volumes of 4 and 6 OM's peaked at just below 3 OM's of present day mantle water volumes (Figure 8a). Paths that started with an initial mantle water volume of 2 OM's did not end in a similar range, as there was not enough water available. Present day surface water volumes split into groups based on the amount of assumed initial mantle water (Figure 8b). This is not a surprise. Model feedbacks can regulate internal mantle water volumes, but the model has no such feedbacks that would regulate surface water volumes. As such, final surface water volumes are more strongly dependent on assumed initial water volumes. In our analysis, we did not account for any initial surface water or late stage water addition. If we did, models that assumed an initial condition of 2 OM's water volumes could potentially match present day surface water volume. We also did not account for surface water loss to space over model evolution times. If we did, models that assumed an initial condition of greater than 4 OM volumes could also potentially match present day water volumes. With those two caveats, the assumed 4 OM initial condition does most closely satisfy the present day surface water constraint.

We conclude this section by plotting mantle water volume and mantle temperature over time for all successful models (Figure 9). Figure 9a shows that the mantle water volumes collapsed to a relatively narrow range over the age of the Earth for most models. The exceptions being cases that began with 2 OM's of water. This supports the idea that internal mantle feedbacks regulate the amount of water in the mantle. Figure 9b shows the range of successful thermal paths satisfying all constraints. There are two dis-

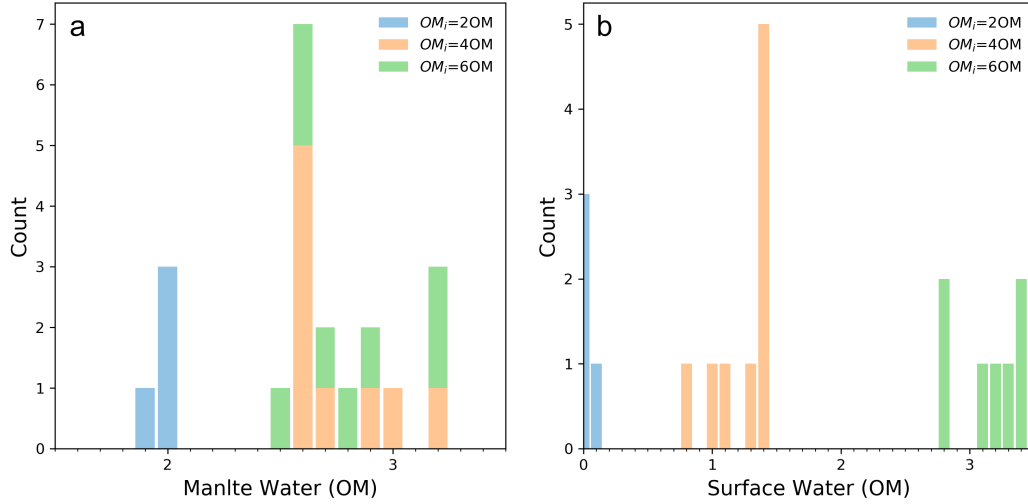


Figure 8. Present day mantle (a) and surface (b) water volumes, in present day ocean masses, for model paths that matched all constraints. Histogram is colored coded by the amount of water that was assumed as an initial condition.

tinguishable groups: those that start warm and those that start cooler. Both groups lead to multi-stage cooling paths but of different natures. The models that started cooler experienced a mantle heating stage followed by cooling. The models that started warmer experienced a reduced cooling stage between 4.0 to 2.5 Ga followed by accelerated mantle cooling. It is interesting to note that the warm start trend is in line with the conceptual interpretation of the paleo temperature data offered by Condie et al. (2016) while the cooler start is consistent with the interpretation of Herzberg et al. (2010).

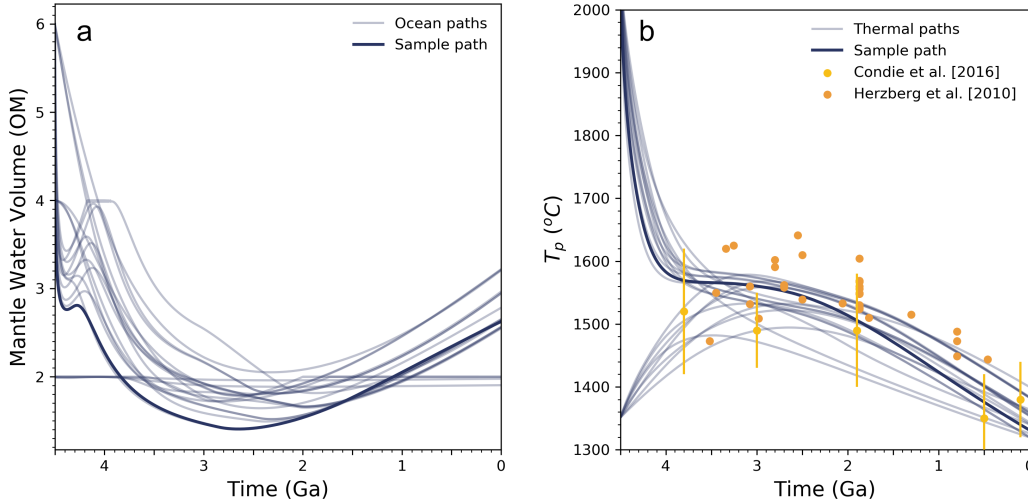


Figure 9. Mantle water volume (a) and thermal (b) paths that matched all constraints. In (b) we show paleo thermal history estimates that suggest a multi-phase thermal history along with successful thermal paths for qualitative comparison with the output of our analysis.

3.3 Feedback Analysis

In this section we provide further support that a multi-stage thermal history can result from changes in the deep water cycle. For clarity, we focus on the path highlighted in Figure 9b.

Figure 10 shows the relative and absolute influences of the deep water cycle and thermal effects on mantle viscosity. The dark red line shows how the deep water cycle changed mantle viscosity with time ($\eta_{\chi}\dot{\chi}_m$), and the light red line shows how thermal effects changed mantle viscosity with time ($\eta_T\dot{T}$). The black line (S_{WT}) is the ratio of $\eta_{\chi}\dot{\chi}_m$ to $\eta_T\dot{T}$. The first 0.8 billion years of the thermal history was characterized by $S_{WT} < 1$. Over half of that stage $S_{WT} < 0.1$. This indicates that thermal effects dominated the overall system feedback. The second stage of the thermal history began at roughly 4 Ga when S_{WT} grew larger than one. This persisted until ~ 2.8 Ga. During this stage, S_{WT} peaked at 3.6 Ga, indicating a fundamental change to the overall model feedback structure. This coincided with a minimum in $\eta_T\dot{T}$. The third stage, with S_{WT} again dropping below unity, lasted from 2.8 Ga to present. Early in this phase, at ~ 2.7 Ga, the deep water cycle experienced a dramatic shift: the net flow of water began to enter rather than exit the mantle. The change to a rehydrating mantle means the water cycle tended to lower mantle viscosity which, in turn, tended to enhance mantle cooling. The timing of the shift in water cycling is expressed in Figure 10 by $\eta_{\chi}\dot{\chi}_m$ dropping below zero. During this last stage, S_{WT} approached one as both $\eta_{\chi}\dot{\chi}_m$ and $\eta_T\dot{T}$ grew quickly but in opposing directions. This ended abruptly when the maximum dehydrated layer thickness was reached at 1.6 Ga, and S_{WT} slowly drifted towards lower values.

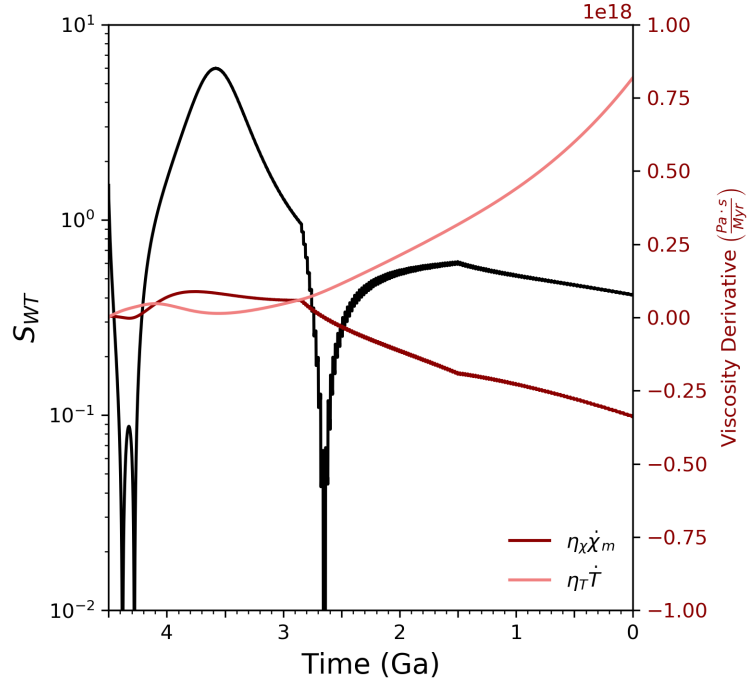


Figure 10. Quantitative analysis of feedbacks. When $S_{WT} > 1$, water cycling influence mantle viscosity ($\eta_{\chi}\dot{\chi}_m$) more than thermal effects ($\eta_T\dot{T}$).

The feedback analysis of Figure 10, and associated model trends of Figure 9, provide insights into the competing factors that allow for the three thermal history stages discussed.

During the first stage, the strong negative feedback associated with the thermal loop caused rapid adjustment from an initially hot or cool start (Figure 9b). This worked to bring heat flow and radiogenic heat production toward a balance. In this sense, the model behavior was not drastically different than classic thermal history models with β values near 0.3 (Tozer, 1972; Schubert et al., 1980; Spohn & Schubert, 1982; Jackson & Pollack, 1984). This is consistent with S_{WT} being below 0.1 over much of this stage (Figure 10).

As heat flow and radiogenic heat production approached a balance, water cycling effects on mantle viscosity could start to compete with the negative thermal feedback. This marked the start of the second thermal history stage. The mantle was degassing during this stage (Figure 9b). This worked to stiffen the mantle. This, on its own, tended to drive less efficient mantle convection and associated heating. However, radiogenics in the mantle were decaying and producing less heat which allowed for a balance between hydration and thermal feedbacks. As a result, a stage of relatively mild mantle cooling could be maintained. As the mantle continued to dehydrate, the solidus shifted to warmer temperatures. This reduced the melt fraction and slowed the rate at which water was lost from the mantle. This limited the peak of the water cycling effect during the second stage. As a result, the flat line temperature trend could not be maintained and the mantle started to progressively cool. The geotherm moved towards the solidus, further reducing melt volumes. Cooling also thickened the lithosphere and the thickness of the hydrated layer within it. This started to deliver more water back into the mantle. This further damped the rate at which water was lost. With this process set in motion, the second stage gave way to the final thermal history stage.

During the third stage, water cycling transitioned to net rehydration of the mantle. This caused a change from water cycling tending to stiffen the mantle to water cycling tending to weaken the mantle (Figure 10). Thermal effects on viscosity were stronger than water effects but the two were not strongly out of balance (Figure 10). As such, both contributed to the overall trend in the final stage, particularly over the first ~ 1 billion years of the third stage. As the mantle cooled, the geotherm shifted further towards the solidus and the melt zone began to shrink. This reduced the melt fraction, which allowed less water to leave the mantle. The lithosphere continued to thicken as did the hydrated layer embedded within it. This increased the rate at which water was delivered into the mantle. The combined effects of a shrinking melt zone and increased delivery of water into the mantle lead to a mild rise in the water cycling effect over the start of the third stage (Figure 10). That rise ended once the hydrated lithosphere layer reached its maximum allowable thickness. If this limit did not exist, then S_{WT} could have continued its mild rise but it would have remained below unity as the rise in thermal effects exceeded it. With the limit in place, net rehydration of the mantle, and associated decline of surface water, slowed. None the less, both thermal and water cycling effects continued to influence thermal history with the thermal effect being stronger by a factor of ~ 2 at a model time representing present day (Figure 10).

4 Discussion

A three stage thermal history, as analyzed in the previous section, is consistent with geologic proxy data and can match present day constraints. Figure 11 shows the uncertainties of our successful model paths projected onto the paleo temperature proxy data. We calculated the mean and two-sigma uncertainty bounds for the 21 thermal paths that satisfied all constraints. The time domain spans from the present day to 4 Ga, as this is the extent of the proxy data. However, in all of our models, the second thermal his-

tory stage began prior to 4 Ga. Within model uncertainties, the second stage is predicted to extended to 3.5-2 Ga. The mean of the uncertainty window predicts that a transition to stage three occurs at ~ 2.7 Ga. That transition is associated with a change from net mantle degassing to net regassing. Collectively, our results argue that paleo temperature data is not necessarily indicative of a change in tectonic regime (Condie et al., 2016). Changes in the deep water cycling can account for the data and for present day data constraints. This provides a viable alternative hypothesis.

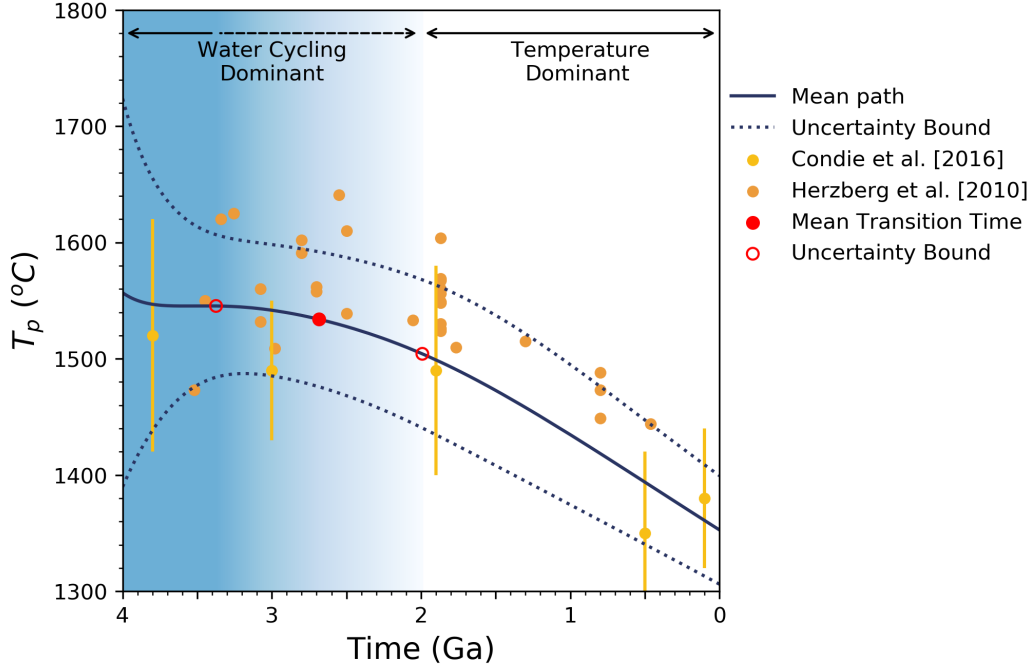


Figure 11. Summary of all results and uncertainties. We show the mean and two-sigma uncertainty of model paths that matched all constraints. The red dots indicate the mean and uncertainty of the change from water cycling (phase two) to thermal dominance (phase three) of the thermal history. This change in phase coincided with the change in slope of both paleo mantle temperature estimates, suggesting our hypothesis is viable and that there is no need to invoke a change in convective regime.

Using data constraints to eliminate potential model paths also provided us with a β value range that allowed for successful model paths. Figure 7 indicates that the range is $0.25 \leq \beta \leq 0.3$. We can compare that with results from thermal history models that do not include deep water cycling. Seales and Lenardic (2020) systematically explored a range of such models and subjected them to the same thermal constraints used herein. The probability density function for successful models spanned a wider range than that of Figure 7. It was also double peaked with a mild peak at $\beta = -0.10$ and a stronger peak at $\beta = 0.15$. Both those peaks are associated with models that assume that plate and/or plate margin strength provides the primary Resistance to plate motions (Conrad & Hager, 1999b; Korenaga, 2003). Our results, on the other hand, suggest that mantle viscosity primarily resists plate motions.

The principal reason for the different modeling conclusions noted above is that the study of this paper coupled deep water cycling to thermal history. This allowed us to add the constraint that deep water cycling transitions from net mantle dehydration to

net rehydration over geologic time. The time window of the transition, within model uncertainty, that we predict is in line with observational constraints (Parai & Mukhopadhyay, 2018). Not surprisingly, adding a new constraint lead to a lower overall number of successful model paths than was determined by the study of Seales and Lenardic (2020). There is another difference that should be noted from our approach and an alternative modeling methodology. Some thermal history modeling approaches build present day thermal constraints directly into the models and calculate model paths in "reverse time" starting from the present and extending to the past (Christensen, 1985; Korenaga, 2003). We did not follow this approach. This allowed us to use present day constraints to eliminate model paths rather than build the constraints into the model. This had a critical effect on our viable β range. Models with lower values of β struggled to match present day temperatures (Figure 5a). This is consistent with McNamara and Van Keken (2000) who found that lower β value models tended to run too hot.

It is worth specifically comparing our model to another thermal history model that also invoked hydration effects but in a very different way. Korenaga (2003) took the view that plates rather than mantle viscosity primarily resist plate motions. The associated model they explored assumed that an elevated mantle temperature produces larger melt volumes which, in turn, creates a thicker dehydrated lithosphere in the Earth's past. This leads to thicker and stronger plates further back in geologic time. The thicker and stronger plates impeded plate motions and associated mantle cooling. Korenaga (2003) determined that an effective β value of -0.15 could capture these effects within a thermal history model. This is different from the models herein which assumed that mantle viscosity provides the principal resistance to plate motion. As noted in the introduction, this was motivated, in part, by studies that have argued against the physical viability of negative β models (Gerardi et al., 2019).

Future extension of our models could include effects we did not directly model. Chotalia et al. (2020) showed that including a finite delay in the mixing time for water in the mantle could affect hydration feedbacks on the solidus at the mid-ocean ridge. They found that when they included this delay, it restricted the period of mantle regassing. It also opened up the possibility for shorter timescale oscillations between mantle regassing and degassing states. Karlsen et al. (2019) also found that a perturbed water cycle, this time by supercontinental breakup, could perturb sea-level by more than 100 m. In both cases, the added model complexities lead to fluctuations about mean trends. Thermal history models traditionally have tracked mean values over time and it has been noted that fluctuations about the mean are to be expected and that should be considered when evaluating thermal history model results (Lenardic et al., 2016; Silver & Behn, 2008). Although we did not consider the specific effects noted above in our analysis, we did consider the role of unmodeled effects, and associated fluctuations about mean trends, when we evaluated structural uncertainty (Seales et al., 2019). Models, by definition of the word model, will exclude some physical factors and the value of a structural uncertainty analysis is that it can test the robustness of first-order model trends in the face of this. The fact that the models presented herein are structurally stable goes hand in hand with the robustness of mean trends to potential fluctuations (Figure 4b).

Our results, as related to changes in deep water cycling, have implications extending beyond mantle cooling. The change from stage two to stage three, for our successful thermal history models, is associated with a switch to net regassing of the mantle. The sequence of events that led to this involved the solidus shifting to warmer temperatures below mid-ocean ridges as melting dehydrated the mantle. Simultaneously, heat flow from the mantle decreased, which thickened lithospheric plates. This thickened the hydrated layer that carried water back into the mantle. This implies a switch from relatively dry to wet subduction. Increased water volume delivered into the mantle by subducting slabs could preferentially produce felsic rather than mafic crust. This would increase the area of Earth's surface covered by felsic crust. As a result, its oxidative ef-

635 efficiency would decrease, leading to a rise in atmospheric O₂ (Lee et al., 2016). The ex-
 636 posure of larger felsic areas would allow for higher weathering rates, which could enhance
 637 an influx of carbonates that would further bolster this rise in O₂ (Eguchi et al., 2020).
 638 Our hypothesis predicts, then, that a rise in atmospheric O₂ should coincide with the
 639 timing of the deep water cycle changing convective efficiency and the associated change
 640 in the cooling rate of the mantle. Our models predicts that this change occurs at a mean
 641 model uncertainty time of ~2.7 Ga. This coincides with the inferred timing of the Great
 642 Oxidation Event (e.g., Lyons et al., 2014).

643 5 Conclusions

644 We have used coupled models of deep water cycling and thermal history to explore
 645 the hypothesis that changes in water cycling, over geologic time, could lead to multi-stage
 646 mantle cooling. We tested the viability of this hypothesis by applying observational con-
 647 straints on a wide range of calculated model paths. The hypothesis was shown to be com-
 648 patible with data constraints and it did not require changes in the tectonic style of the
 649 Earth over geologic time. It also implied that mantle viscosity provides the dominant
 650 resistance to plate motions with plate and plate margin strength playing a lesser role.

651 Acknowledgments

652 Enter acknowledgments, including your data availability statement, here.

653 References

- 654 Astrom, K. J. K. J., & Murray, R. M. (2008). *Feedback systems: an introduction for*
 655 *scientists and engineers*. Princeton University Press. Retrieved from [https://](https://press.princeton.edu/titles/8701.html)
 656 press.princeton.edu/titles/8701.html doi: 10.5860/choice.46-2107
- 657 Carter, N. L., & Ave'lallemant, H. G. (1970, aug). High Temperature Flow of
 658 Dunite and Peridotite. *Geological Society of America Bulletin*, 81(8), 2181.
 659 Retrieved from [https://pubs.geoscienceworld.org/gsa/gsabulletin/](https://pubs.geoscienceworld.org/gsa/gsabulletin/article/81/8/2181/6919)
 660 [article/81/8/2181/6919](https://pubs.geoscienceworld.org/gsa/gsabulletin/article/81/8/2181/6919) doi: 10.1130/0016-7606(1970)81[2181:htfoda]2.0.co;
 661 2
- 662 Chopra, P. N., & Paterson, M. S. (1984, sep). The role of water in the defor-
 663 mation of dunite. *Journal of Geophysical Research*, 89(B9), 7861–7876.
 664 Retrieved from <http://doi.wiley.com/10.1029/JB089iB09p07861> doi:
 665 10.1029/JB089iB09p07861
- 666 Chotalia, K., Cagney, N., Lithgow-Bertelloni, C., & Brodholt, J. (2020, jan).
 667 The coupled effects of mantle mixing and a water-dependent viscosity on
 668 the surface ocean. *Earth and Planetary Science Letters*, 530, 115881. Re-
 669 trieved from [https://www.sciencedirect.com/science/article/pii/](https://www.sciencedirect.com/science/article/pii/S0012821X19305734)
 670 [S0012821X19305734](https://www.sciencedirect.com/science/article/pii/S0012821X19305734) doi: 10.1016/J.EPSL.2019.115881
- 671 Christensen, U. R. (1984, nov). Heat transport by variable viscosity convection and
 672 implications for the Earth's thermal evolution. *Physics of the Earth and Plan-*
 673 *etary Interiors*, 35(4), 264–282. Retrieved from [https://www.sciencedirect](https://www.sciencedirect.com/science/article/pii/0031920184900219)
 674 [.com/science/article/pii/0031920184900219](https://www.sciencedirect.com/science/article/pii/0031920184900219) doi: 10.1016/0031-9201(84)
 675 90021-9
- 676 Christensen, U. R. (1985, mar). THERMAL EVOLUTION MODELS FOR
 677 THE EARTH. *Journal of Geophysical Research*, 90(B4), 2995–3007. Re-
 678 trieved from <http://doi.wiley.com/10.1029/JB090iB04p02995> doi:
 679 10.1029/JB090iB04p02995
- 680 Condie, K. C., Aster, R. C., & Van Hunen, J. (2016). A great thermal diver-
 681 gence in the mantle beginning 2.5 Ga: Geochemical constraints from green-
 682 stone basalts and komatiites. *Geoscience Frontiers*, 7(4), 543–553. Re-
 683 trieved from <http://dx.doi.org/10.1016/j.gsf.2016.01.006> doi:

- 10.1016/j.gsf.2016.01.006
- Conrad, C. P., & Hager, B. H. (1999a). Effects of plate bending and fault strength at subduction zones on plate dynamics. *Journal of Geophysical Research: Solid Earth*, 104(B8), 17551–17571. Retrieved from <http://onlinelibrary.wiley.com/doi/10.1029/1999JB900149/full> doi: 10.1029/1999jb900149
- Conrad, C. P., & Hager, B. H. (1999b, oct). The thermal evolution of an earth with strong subduction zones. *Geophysical Research Letters*, 26(19), 3041–3044. Retrieved from <http://doi.wiley.com/10.1029/1999GL005397> doi: 10.1029/1999GL005397
- Crowley, J. W., G rault, M., & O’Connell, R. J. (2011). On the relative influence of heat and water transport on planetary dynamics. *Earth and Planetary Science Letters*, 310(3–4), 380–388. Retrieved from <http://dx.doi.org/10.1016/j.epsl.2011.08.035> doi: 10.1016/j.epsl.2011.08.035
- Davies, G. F. (1980). Thermal histories of convective earth models and constraints on radiogenic heat production in the earth. *Journal of Geophysical Research*, 85(B5), 2517–2530. doi: 10.1029/JB085iB05p02517
- Eguchi, J., Seales, J., & Dasgupta, R. (2020, jan). Great Oxidation and Lomagundi events linked by deep cycling and enhanced degassing of carbon. *Nature Geoscience*, 13(1), 71–76. Retrieved from <http://www.nature.com/articles/s41561-019-0492-6> doi: 10.1038/s41561-019-0492-6
- Ganne, J., & Feng, X. (2017, mar). Primary magmas and mantle temperatures through time. *Geochemistry, Geophysics, Geosystems*, 18(3), 872–888. Retrieved from <http://doi.wiley.com/10.1002/2016GC006787> doi: 10.1002/2016GC006787
- George, D. A. R., & Oxley, L. T. (1985, oct). Structural stability and model design. *Economic Modelling*, 2(4), 307–316. Retrieved from <https://www.sciencedirect.com/science/article/pii/0264999385900264> doi: 10.1016/0264-9993(85)90026-4
- Gerardi, G., Ribe, N. M., & Tackley, P. J. (2019, jun). Plate bending, energetics of subduction and modeling of mantle convection: A boundary element approach. *Earth and Planetary Science Letters*, 515, 47–57. Retrieved from <https://www.sciencedirect.com/science/article/pii/S0012821X1930158X?via=ihub> doi: 10.1016/J.EPSL.2019.03.010
- Giannandrea, E., & Christensen, U. (1993, jun). Variable viscosity convection experiments with a stress-free upper boundary and implications for the heat transport in the Earth’s mantle. *Physics of the Earth and Planetary Interiors*, 78(1–2), 139–152. Retrieved from <https://www.sciencedirect.com/science/article/pii/003192019390090V> doi: 10.1016/0031-9201(93)90090-V
- Grign  , C., & Labrosse, S. (2001, jul). Effects of continents on earth cooling: Thermal blanketing and depletion in radioactive elements. *Geophysical Research Letters*, 28(14), 2707–2710. Retrieved from <http://doi.wiley.com/10.1029/2000GL012475> doi: 10.1029/2000GL012475
- Guckenheimer, J., & Holmes, P. J. (1983). *Nonlinear Oscillations, Dynamical Systems, and Bifurcations of Vector Fields*. New York, NY: Springer New York. Retrieved from <http://link.springer.com/10.1007/978-1-4612-1140-2> doi: 10.1007/978-1-4612-1140-2
- Gurnis, M. (1989, feb). A reassessment of the heat transport by variable viscosity convection with plates and lids. *Geophysical Research Letters*, 16(2), 179–182. Retrieved from <http://doi.wiley.com/10.1029/GL016i002p00179> doi: 10.1029/GL016i002p00179
- Herzberg, C., Condie, K., & Korenaga, J. (2010, mar). Thermal history of the Earth and its petrological expression. *Earth and Planetary Science Letters*, 292(1–2), 79–88. Retrieved from <https://www.sciencedirect.com/science/article/pii/S0012821X10000567> doi: 10.1016/j.epsl.2010.01.022

- Hirschmann, M. M. (2000, oct). Mantle solidus: Experimental constraints and the effects of peridotite composition. *Geochemistry, Geophysics, Geosystems*, 1(10). Retrieved from <https://agupubs.onlinelibrary.wiley.com/doi/full/10.1029/2000GC000070> doi: 10.1029/2000GC000070
- Hirth, G., & Kohlstedt, D. L. (1996, oct). Water in the oceanic upper mantle: Implications for rheology, melt extraction and the evolution of the lithosphere. *Earth and Planetary Science Letters*, 144(1-2), 93–108. Retrieved from <https://www.sciencedirect.com/science/article/pii/0012821X96001549> doi: 10.1016/0012-821x(96)00154-9
- Höink, T., Jellinek, A. M., & Lenardic, A. (2011, oct). Viscous coupling at the lithosphere-aesthenosphere boundary. *Geochemistry, Geophysics, Geosystems*, 12(10), n/a–n/a. Retrieved from <http://doi.wiley.com/10.1029/2011GC003698> doi: 10.1029/2011GC003698
- Höink, T., Lenardic, A., & Jellinek, A. M. (2013, aug). *Earth's thermal evolution with multiple convection modes: A Monte-Carlo approach* (Vol. 221). Elsevier. Retrieved from <https://www.sciencedirect.com/science/article/pii/S0031920113000812> doi: 10.1016/j.pepi.2013.06.004
- Jackson, M. J., & Pollack, H. N. (1984, nov). on the Sensitivity of Parameterized Convection To the Rate of Decay of Internal Heat Sources. *Journal of Geophysical Research*, 89(B12), 10103–10108. Retrieved from <http://doi.wiley.com/10.1029/JB089iB12p10103> doi: 10.1029/JB089iB12p10103
- Jaupart, C., Labrosse, S., & Mareschal, J. C. (2007). *Temperatures, Heat and Energy in the Mantle of the Earth* (Vol. 7) (No. February). Elsevier B.V. Retrieved from <http://dx.doi.org/10.1016/B978-0-444-53802-4.00126-3> doi: 10.1016/B978-044452748-6.00114-0
- Karato, S. I., & Wu, P. (1993). Rheology of the upper mantle: A synthesis. *Science*, 260(5109), 771–778. Retrieved from <https://www.jstor.org/stable/2881160?seq=1#metadata-abstract-info-tab-contents> doi: 10.1126/science.260.5109.771
- Karlsen, K. S., Conrad, C. P., & Magni, V. (2019). Deep Water Cycling and Sea Level Change Since the Breakup of Pangea. *Geochemistry, Geophysics, Geosystems*, 20(6), 2919–2935. doi: 10.1029/2019GC008232
- Katz, R. F., Spiegelman, M., & Langmuir, C. H. (2003). A new parameterization of hydrous mantle melting. *Geochemistry, Geophysics, Geosystems*, 4(9), 1–19. doi: 10.1029/2002GC000433
- Korenaga, J. (2003). Energetics of mantle convection and the fate of fossil heat. *Geophysical Research Letters*, 30(8), 47–63. doi: 10.1029/2003GL016982
- Lee, C.-T. A., Yeung, L. Y., McKenzie, N. R., Yokoyama, Y., Ozaki, K., & Lenardic, A. (2016). Two-step rise of atmospheric oxygen linked to the growth of continents. *Nature Geoscience*, 9(6), 417–424. Retrieved from <http://dx.doi.org/10.1038/ngeo2707> doi: 10.1038/ngeo2707
- Lenardic, A., Cooper, C. M., & Moresi, L. (2011). A note on continents and the Earth's Urey ratio. *Physics of the Earth and Planetary Interiors*, 188(1-2), 127–130. doi: 10.1016/j.pepi.2011.06.008
- Lenardic, A., Jellinek, A. M., Foley, B., O'Neill, C., & Moore, W. B. (2016). *Climate-tectonic coupling: Variations in the mean, variations about the mean, and variations in mode*. doi: 10.1002/2016JE005089
- Lenardic, A., & Moresi, L. (2003, feb). Thermal convection below a conducting lid of variable extent: Heat flow scalings and two-dimensional, infinite Prandtl number numerical simulations. *Physics of Fluids*, 15(2), 455–466. Retrieved from <http://aip.scitation.org/doi/10.1063/1.1533755> doi: 10.1063/1.1533755
- Li, Z.-X. A., Lee, C.-T. A., Peslier, A. H., Lenardic, A., & Mackwell, S. J. (2008,

- 794 sep). Water contents in mantle xenoliths from the Colorado Plateau and
 795 vicinity: Implications for the mantle rheology and hydration-induced thin-
 796 ning of continental lithosphere. *Journal of Geophysical Research*, 113(B9),
 797 B09210. Retrieved from <http://doi.wiley.com/10.1029/2007JB005540> doi:
 798 10.1029/2007JB005540
- 799 Lyons, T. W., Reinhard, C. T., & Planavsky, N. J. (2014, feb). The rise of oxy-
 800 gen in Earth's early ocean and atmosphere. *Nature*, 506(7488), 307–315. Re-
 801 trieved from <http://www.nature.com/articles/nature13068> doi: 10.1038/
 802 nature13068
- 803 Mackwell, S. J., Kohlstedt, D. L., & Paterson, M. S. (1985, nov). The role of
 804 water in the deformation of olivine single crystals. *Journal of Geophysical*
 805 *Research*, 90(B13), 11319. Retrieved from <http://doi.wiley.com/10.1029/JB090iB13p11319> doi: 10.1029/jb090ib13p11319
- 806 McNamara, A. K., & Van Keken, P. E. (2000, nov). Cooling of the Earth: A param-
 807 eterized convection study of whole versus layered models. *Geochemistry, Geo-*
 808 *physics, Geosystems*, 1(11), n/a–n/a. Retrieved from [http://doi.wiley.com/](http://doi.wiley.com/10.1029/2000GC000045)
 809 [10.1029/2000GC000045](http://doi.wiley.com/10.1029/2000GC000045) doi: 10.1029/2000GC000045
- 810 Mei, S., & Kohlstedt, D. L. (2000, sep). Influence of water on plastic deformation
 811 of olivine aggregates: 2. Dislocation creep regime. *Journal of Geophysical Re-*
 812 *search: Solid Earth*, 105(B9), 21471–21481. Retrieved from [http://doi.wiley](http://doi.wiley.com/10.1029/2000JB900180)
 813 [.com/10.1029/2000JB900180](http://doi.wiley.com/10.1029/2000JB900180) doi: 10.1029/2000jb900180
- 814 Moore, W. B., & Lenardic, A. (2015, nov). The efficiency of plate tectonics and
 815 nonequilibrium dynamical evolution of planetary mantles. *Geophysical Re-*
 816 *search Letters*, 42(21), 9255–9260. Retrieved from [http://doi.wiley.com/](http://doi.wiley.com/10.1002/2015GL065621)
 817 [10.1002/2015GL065621](http://doi.wiley.com/10.1002/2015GL065621) doi: 10.1002/2015GL065621
- 818 Moresi, L., & Solomatov, V. (1998, jun). Mantle convection with a brit-
 819 tle lithosphere: thoughts on the global tectonic styles of the Earth and
 820 Venus. *Geophysical Journal International*, 133(3), 669–682. Retrieved
 821 from [https://academic.oup.com/gji/article-lookup/doi/10.1046/](https://academic.oup.com/gji/article-lookup/doi/10.1046/j.1365-246X.1998.00521.x)
 822 [j.1365-246X.1998.00521.x](https://academic.oup.com/gji/article-lookup/doi/10.1046/j.1365-246X.1998.00521.x) doi: 10.1046/j.1365-246X.1998.00521.x
- 823 Parai, R., & Mukhopadhyay, S. (2018, aug). Xenon isotopic constraints on the his-
 824 tory of volatile recycling into the mantle. *Nature*, 560(7717), 223–227. Re-
 825 trieved from <http://www.nature.com/articles/s41586-018-0388-4> doi: 10
 826 .1038/s41586-018-0388-4
- 827 Rüpke, L. H., Morgan, J. P., Hort, M., & Connolly, J. A. (2004, jun). Serpentine
 828 and the subduction zone water cycle. *Earth and Planetary Science Letters*,
 829 223(1-2), 17–34. Retrieved from [https://www.sciencedirect.com/science/](https://www.sciencedirect.com/science/article/pii/S0012821X04002663)
 830 [article/pii/S0012821X04002663](https://www.sciencedirect.com/science/article/pii/S0012821X04002663) doi: 10.1016/j.epsl.2004.04.018
- 831 Sandu, C., Lenardic, A., & McGovern, P. (2011). The effects of deep water cycling
 832 on planetary thermal evolution. *Journal of Geophysical Research: Solid Earth*,
 833 116(12), 1–15. doi: 10.1029/2011JB008405
- 834 Schubert, G., & Anderson, C. A. (1985, mar). Finite element calculations of very
 835 high Rayleigh number thermal convection. *Geophysical Journal of the Royal*
 836 *Astronomical Society*, 80(3), 575–601. Retrieved from [https://academic](https://academic.oup.com/gji/article-lookup/doi/10.1111/j.1365-246X.1985.tb05112.x)
 837 [.oup.com/gji/article-lookup/doi/10.1111/j.1365-246X.1985.tb05112.x](https://academic.oup.com/gji/article-lookup/doi/10.1111/j.1365-246X.1985.tb05112.x)
 838 doi: 10.1111/j.1365-246X.1985.tb05112.x
- 839 Schubert, G., Cassen, P., & Young, R. E. (1979). Subsolidus convective cooling his-
 840 tories of terrestrial planets. *Icarus*, 38(2), 192–211. doi: 10.1016/0019-1035(79)
 841 90178-7
- 842 Schubert, G., Stevenson, D., & Cassen, P. (1980). Whole Planet Cooling and the
 843 Radiogenic Heat Source Contents of the Earth and Moon. *Journal of Geophys-*
 844 *ical Research*, 85(B5), 2531–2538.
- 845 Schubert, G., Turcotte, D. L., & Olson, P. (2001). *Mantle Convection in the*
 846 *Earth and Planets*. Cambridge University Press. Retrieved from [https://](https://www.cambridge.org/core/product/identifier/9780511612879/type/book)
 847 www.cambridge.org/core/product/identifier/9780511612879/type/book

- doi: 10.1017/cbo9780511612879
- Seales, J., & Lenardic, A. (2020). Uncertainty Quantification in Planetary Thermal History Models: Implications for Hypotheses Discrimination and Habitability Modeling. *The Astrophysical Journal, In Press*.
- Seales, J., Lenardic, A., & Moore, W. B. (2019, aug). Assessing the Intrinsic Uncertainty and Structural Stability of Planetary Models: 1. Parameterized Thermal-Tectonic History Models. *Journal of Geophysical Research: Planets*, 124(8), 2213–2232. Retrieved from <https://onlinelibrary.wiley.com/doi/abs/10.1029/2019JE005918> doi: 10.1029/2019je005918
- Silver, P. G., & Behn, M. D. (2008, jan). Intermittent plate tectonics? *Science*, 319(5859), 85–88. Retrieved from <http://www.ncbi.nlm.nih.gov/pubmed/18174440> doi: 10.1126/science.1148397
- Spohn, T., & Schubert, G. (1982, jun). Modes of mantle convection and the removal of heat from the earth’s interior. *Journal of Geophysical Research*, 87(B6), 4682–4696. Retrieved from <http://doi.wiley.com/10.1029/JB087iB06p04682> doi: 10.1029/JB087iB06p04682
- Strong, M., & Oakley, J. E. (2014). When Is a Model Good Enough? Deriving the Expected Value of Model Improvement via Specifying Internal Model Discrepancies. *SIAM/ASA Journal on Uncertainty Quantification*, 2(1), 106–125. Retrieved from <http://www.siam.org/journals/juq/2/88956.html> doi: 10.1137/120889563
- Tozer, D. C. (1972). The present thermal state of the terrestrial planets. *Physics of the Earth and Planetary Interiors*, 6(1-3), 182–197. Retrieved from https://ac.els-cdn.com/0031920172900520/1-s2.0-0031920172900520-main.pdf?{_}tid=27e5fb72-6b52-46c9-85ac-cc6a4cdb1f74{\&}acdnat=1540245334{_}fd78e73ff73e0fea7946f20a31722e0b doi: 10.1016/0031-9201(72)90052-0
- Ulmer, P., & Trommsdorff, V. (1995). Serpentine Stability to Mantle Depths and Subduction-Related Magmatism. *Science*, 268(5212), 858–861. Retrieved from <http://www.sciencemag.org/cgi/doi/10.1126/science.268.5212.858> doi: 10.1126/science.268.5212.858
- Weertman, J., & Weertman, J. R. (1975, may). High Temperature Creep of Rock and Mantle Viscosity. *Annual Review of Earth and Planetary Sciences*, 3(1), 293–315. Retrieved from <http://www.annualreviews.org/doi/10.1146/annurev.ea.03.050175.001453> doi: 10.1146/annurev.ea.03.050175.001453
- Weller, M. B., & Kiefer, W. S. (2020). The Physics of Changing Tectonic Regimes: Implications for the Temporal Evolution of Mantle Convection and the Thermal History of Venus. *Journal of Geophysical Research: Planets*, 125(1), 1–22. doi: 10.1029/2019JE005960
- Wieder, W. R., Cleveland, C. C., Lawrence, D. M., & Bonan, G. B. (2015, apr). Effects of model structural uncertainty on carbon cycle projections: Biological nitrogen fixation as a case study. *Environmental Research Letters*, 10(4), 044016. Retrieved from <http://stacks.iop.org/1748-9326/10/i=4/a=044016?key=crossref.27ff2d3c016ebe5e184f5d9334a5791f> doi: 10.1088/1748-9326/10/4/044016